As-Built Geometry Imperfections and Misalignments in Maritime Structures

A Probabilistic Approach to Fatigue Assessment

By

Sjors Kremer

to obtain the degree of

Master of Science
in Offshore and Dredging Engineering
with a specialization in Structural Analysis and Design
at Delft University of Technology

to be defended publicly on Thursday October 9, 2025

Student number: 4963369

Thesis committee:			
	Dr. ir. J.H. den Besten	TU Delft	Chairman
	Ir. R.L.G. Slange	TU Delft	Supervisor
	Ir. P.T. Nobel	Nevesbu B.V.	Supervisor
	Prof. dr. M. Veljkovic	TU Delft	

As-Built Geometry Imperfections and Misalignments in Maritime Structures: A Probabilistic Approach to Fatigue Assessment

S. Kremer[a,b], R.L.G. Slange[a], J.H. den Besten[a], P.T. Nobel[b] and A. Zambon[b]

[a]*Delft University of Technology, Mekelweg 5, Delft, 2628 CD, The Netherlands*
[b]*Nevesbu B.V. , Kelvinring 48, Alblasserdam, 2952 BG, The Netherlands*

ARTICLE INFO

Keywords:
maritime structures
fatigue
imperfections and misalignments
stress concentration factors
probabilistic framework
spectral representation

ABSTRACT

Fatigue design for maritime structures currently relies on deterministic models of idealised geometries, which do not account for the substantial variability introduced by misalignments and imperfections. A probabilistic framework is presented that models imperfections as spatially varying random fields or random variables, using the Stochastic Hungry Horse model, Spectral Representation Method, Halton sampling, and Bayesian updating. Applied to a finite element model of a stiffened panel with Non-Watertight details, results show that local plate distortions reduce stresses under water pressure but increase them under global hull girder bending. Stiffener distortions govern the Hot Spots at the Non-Watertight details, producing both tensile and compressive stress concentration factors. Comparison with guidelines indicates that current safety factors are non-conservative, as secondary bending effects are not addressed. The framework captures fabrication- and assembly-induced variability and supports data-driven refinement of fatigue criteria.

1. Introduction

Maritime structures are continuously exposed to cyclic loading and response conditions due to e.g. waves, wind and equipment. Fatigue is a cyclic loading and response-induced mechanism that causes localized, progressive structural damage, ultimately resulting in fracture [1]. As such, fatigue is a governing limit state for such structures and accounts for a large proportion of failures [2]. Traditionally, the structural member assemblies of maritime structures are connected by (arc-) welded joints. Local (arc-)welded geometries often exhibit geometric discontinuities, i.e. notches, that act as local stress raisers, accelerating crack initiation and growth under repeated loading cycles [3, 4, 5]. Ensuring accurate fatigue performance therefore requires a thorough treatment of the uncertainties that are inherent to all structural modelling approaches.

Structural assemblies in maritime structures comprise a broad range of structural components and details. The combination of involved fabrication and assembly processes, including workmanship and welding processes, unequivocally leads to various misalignments and imperfections. In general, misalignments and imperfections can be categorised as (1) non-uniform material properties, (2) welding-induced subsurface imperfections, (3) in-service degradations, (4) welding-induced distortions and (5) workmanship-induced misalignments. The focus of this work is specifically on deviations from the idealised geometry caused either by welding or poor workmanship. To narrow the range of potential misalignments and imperfections, the scope is restricted to the orthotropic stiffened panel configuration typical of maritime structures.

While the terms misalignment and imperfection are often used interchangeably, the following definitions are adopted to ensure a clear distinction between the two. *Misalignments* refer to the deviations of structural components from their intended relative positions as a result of the assembly process, including both angular and linear misalignments. *Geometric imperfections* refer to the deviation of an individual structural member from its idealized geometry. Such imperfections typically originate from the fabrication process and may include, for example, weld geometry irregularities and out-of-plane distortions in structural elements. In particular, *distortions* refer to thermally induced deformations caused by the welding process and associated residual stresses

Geometric imperfections and misalignments are a primary concern because, in an imperfect geometry, the local neutral axis is shifted relative to that of the idealised geometry. This shift induces a straightening effect under in-plane tensile loading, generating additional nonlinear secondary bending stresses that influence local hot spot (HS) stresses and, consequently, fatigue strength [6, 7].

As-built misalignments and imperfections remain unknown during the design phase, and explicitly incorporating all such deviations into a finite element model would be a significant effort. Consequently, fatigue assessment methods rely on approaches concerning an idealised, deterministic geometry, where design integrity is assured indirectly through the application of safety factors and conservative $S-N$ curves.

Industry guidelines, including those from DNV [8], BV [9], and ISO [10], incorporate the limit values of assembly tolerances specified in IACS No. 47 [11] and the welding tolerances defined in ISO 5817 [12] into conservative $S-N$ curves and safety factors applied to stress concentration factors (SCFs). However, inspection results consistently

ORCID(s):

show that imperfections and misalignments in as-built structural assemblies often exceed the values assumed during the fatigue testing from which these $S-N$ curves are derived [8, 13]. Furthermore, ISO 5817 [12] classifies weld quality levels that are not technically justified, as their primary purpose is to serve as inspection criteria [14].

This highlights a pronounced disconnect between as-built conditions and their explicit influence on fatigue resistance, underscoring the need to establish a clear and technically justified relationship between them.

Transitioning from current deterministic methodologies to a probabilistic approach allows HS stresses to be represented as distributions rather than fixed values. Such a framework is advantageous because it explicitly incorporates the inherent geometrical randomness of as-built structures, a feature that traditional deterministic assessment methodologies fail to do. Although recent advances have been made in stochastic modelling for the buckling and ultimate strength analysis of plates and shell elements [15], equivalent developments for fatigue assessment remain limited, despite the well-established influence of geometric misalignments and imperfections on fatigue resistance.

Aiming to establish a probabilistic framework for fatigue assessment that explicitly incorporates stochastic imperfections in (arc-)welded maritime structures, relevant misalignments and geometric imperfections for stiffened panel configurations are identified in Section 2. A combination of random variables and random fields, detailed in Section 3, is employed to derive SCF distributions through a benchmark studies in Section 4, conducted using finite element modelling and the `PyMAPDL` interface. This framework expresses SCFs as probability distributions rather than fixed values, enabling a direct evaluation of safety margins.

2. Imperfections and Misalignments

Limiting the scope of this work to a stiffened panel configuration, reduces the range of potential misalignments and imperfections compared to more complex assemblies. Nevertheless, a substantial amount of geometric variation remains. It is therefore essential to distinguish between relevant misalignments, i.e. those expected to affect fatigue strength, and those considered negligible in this context.

ISO 5817 identifies more than 40 types of weld-related imperfections and misalignments, while IACS No. 47 provides assembly tolerances for over 50 types of structural members. Considering the structural hierarchy of a stiffened panel, relevant misalignments and imperfections are categorized at (1) plate level and (2) plate-to-support member level.

2.1. Plate level

The imperfections that relate to the plate geometry are either dimensional variations or welding-induced defects. As this study does not consider variability in material properties, only deviations in plate thickness and initial out-of-plane distortions are included at this hierarchical level.

2.1.1. Plate thickness

In thin-walled open sections, such as stiffened panel configurations, the plate thickness t_p is the dominant parameter influencing the stiffness distribution at plate level. The bending stiffness D is proportional to the cube of the plate thickness, meaning that even small deviations in t_p can significantly affect the structural behaviour.

In addition, both the membrane and bending components of the linearised structural stress are inversely proportional to the plate thickness. Therefore, reduced deviations in t_p relative to the idealised value result in higher local stress levels, which are not captured in current deterministic design models. The critical influence of plate thickness on stiffness and stress levels justifies the inclusion of t_p as a parameter in this work.

2.1.2. Out-of-plane distortion

It is well established that plates distort as a result of the welding process [16, 17, 18, 19, 20, 21]. This out-of-plane plate distortion shifts the neutral axis from the original symmetry plane, leading to additional secondary bending stresses particularly when subjected to in-plane tensile stresses. While out-of-plane plate distortions have been widely investigated in terms of their effect on buckling behaviour, their role in fatigue strength has seen limited attention.

Distortion profile

A wide variety of distortion profiles for plate fields is available in the literature to model initial out-of-plane plate distortions [22], most of which were developed for ultimate strength assessments, where the primary aim is to initiate buckling in a specific mode or to ensure conservative ultimate strength predictions.

Among the various distortion profiles $f_{0,\mathrm{pl}}(x, y)$, the Hungry Horse (HH) mode is particularly relevant, as it is derived from full-scale measurements conducted on board car- and bulk carriers. Originally proposed by Ueda and Yao [19], the HH mode has been validated in several recent studies [17, 20, 21, 22, 23]. It describes the initial plate distortion using a Fourier series composed of eleven components, as defined in Equation 2. The HH mode reflects observed plate behaviour by combining a half sine wave across the breadth b with multiple sine wave components n along the length a [22]. An illustration of the HH mode is provided in Figure 1.

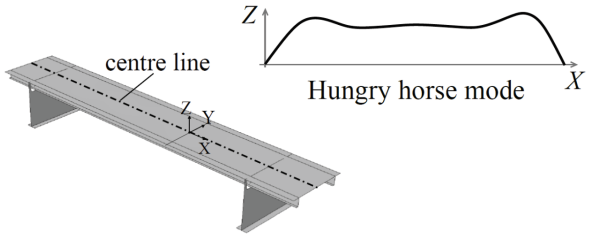

Figure 1: Hungry horse (HH) mode along the plate centre line [24]

$$w_{0,\mathrm{pl}}(x,y) = w_{0,\mathrm{pl}}^{\max} f_{0,\mathrm{pl}}(x,y) \tag{1}$$

$$f_{0,\mathrm{pl}}^{HH}(x,y) = \sum_{n=1}^{11} A_n \sin\left(\frac{n\pi x}{a}\right) \sin\left(\frac{\pi y}{b}\right) \tag{2}$$

The deterministic plate distortion profile $w_{0,\mathrm{pl}}(x,y)$ is defined in Equation 1, where the amplitude $w_{0,\mathrm{pl}}^{\max}$ is determined from the plate slenderness parameter β (Equation 3) following the empirical formulation by Hughes [25]. Equation 4 provides expressions for three severity levels — slight, average, and severe — with comparisons to full-scale measurements indicating that actual distortion magnitudes generally fall between the slight and average levels [26].

$$\beta = \frac{b}{t}\sqrt{\frac{\sigma_Y}{E}} \tag{3}$$

$$w_{0,\mathrm{pl}}^{\max} = \begin{cases} 0.025\beta^2 t_p & \text{for slight level} \\ 0.100\beta^2 t_p & \text{for average level} \\ 0.300\beta^2 t_p & \text{for severe level} \end{cases} \tag{4}$$

Recent studies

Lillemäe [23] examined initial plate distortions in a cruise ship superstructure deck with a plate thickness of 3 mm, modelling various distortion shapes while assuming flat-bar stiffeners, girders, and web frames to be perfectly straight. The study found that, in stiffened panels, a realistic initial distortion shape—and in small welded specimens, both the shape and magnitude significantly influence local stresses near welds. It also noted that nonlinear finite element analysis is of limited priority in large-scale structural models, as the straightening and amplification of initial distortions under global hull girder bending are negligible compared to small-scale specimens.

Similarly, Mancini [27] investigated the fatigue implications of welding-induced plate distortions using 3D laser scan measurements of a stiffened panel cut from a ship-deck demonstrator block ($t_p = 4$ mm), concluding that such distortions must be modelled to accurately predict local weld stresses.

Although both studies focus on relatively thin plates, their findings, combined with the limited attention given to the influence of plate distortions on fatigue strength, underscore the importance of incorporating initial plate distortions in the present study. Neither of the two studies applied a probabilistic method to quantify the influence of these distortions and both relied on deterministic modelling approaches.

2.2. Plate-to-support member level

At the next hierarchical level, plate-to-support member combinations are considered, including plate–stiffener, plate–frame, and plate–girder assemblies. These members, often standardised profiles such as angle bars, tee bars, and bulb flats (commonly referred to as Holland Profiles (HP)), influence both local and global stiffness and can introduce misalignments or imperfections during fabrication. Among their geometric parameters, web height is particularly important due to its contribution to the Steiner term in the moment of inertia; reductions increase flange stresses, often at HS locations. No measurements, tolerances, or statistical data quantifying web height variability are currently available.

2.2.1. Web- and flange distortion

Webs and flanges of stiffening members may also undergo distortions during welding, particularly when flanges are welded rather than hot-rolled. Data on web distortions is scarce, with only one source referenced earlier providing quantitative information. These out-of-plane distortions, in combination with cyclic loading, may cause a phenomenon known as breathing: local flexing during loading and unloading cycles [28]. This effect, illustrated in Figure 2, induces secondary bending stresses that influence local stresses at potential HS locations, motivating the inclusion of stiffener sideways distortion in this study. Similarly, out-of-plane distortions in the flange can also lead to secondary bending stresses.

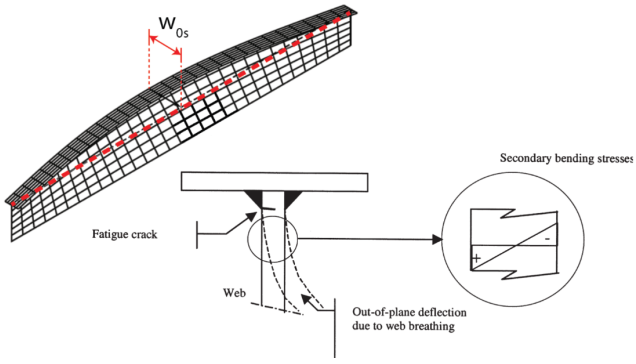

Figure 2: Breathing of stiffener web under cyclic loading [28]

Distortion profile

The sideways distortion of stiffeners, denoted as $w_{0,\mathrm{s}}(x,z)$, is modelled using a maximum distortion magnitude $w_{0,\mathrm{s}}^{\max}$ and a corresponding distortion profile $f_{0,\mathrm{s}}(x,z)$, as defined in Equation 5. The ISSC specifies a maximum distortion magnitude of $w_{0,\mathrm{s}}^{\max} = 0.0015\,a$ (Equation 7), where a is the panel length. The distortion profile is represented as a single sinusoidal half-wave along the stiffener length, with the web distortion increasing linearly from the plate–stiffener connection to its maximum value at the web height h_w, as given in Equation 6.

$$w_{0,\mathrm{s}}(x,z) = w_{0,\mathrm{s}}^{\max} f_{0,\mathrm{s}}(x,z) \tag{5}$$

$$f_{0,s}(x,z) = \frac{z}{h_w} \sin\left(\frac{\pi x}{a}\right) \tag{6}$$

$$w_{0,s}^{\max} = 0.0015\, a \tag{7}$$

The sinusoidal half-wave implies that the deflection profile corresponds to simply-supported boundary conditions. While this assumption may be appropriate in certain cases, it does not represent all structural configurations. In some situations, the boundary conditions more closely resemble those of a clamped–clamped member. To define a distortion profile for such cases, the space-dependent part of the free-vibration solution of an Euler–Bernoulli beam, given in Equation 8, is solved to obtain the formulation of the first mode shape $\Psi(x)$.

$$EI \cdot \frac{\partial^4 w(x,t)}{\partial x^4} + \rho_s A \cdot \frac{\partial^2 w(x,t)}{\partial t^2} = 0 \tag{8}$$

2.2.2. Combined plate-to-support member distortion

Plate-to-support members, as part of a larger structural assembly, can exhibit a characteristic distortion pattern known as a column-type of initial deflection [22, 21]. This distortion, illustrated in Figure 3, represents the combined out-of-plane deformation of the support member and the attached plating. It is typically modelled as a single sinusoidal half-wave in both longitudinal and transverse directions.

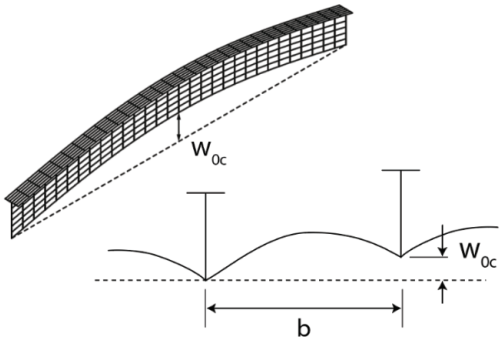

Figure 3: Enter Caption

This column-type distortion, denoted as $w_{0,c}(x,y)$, is modelled using a maximum distortion magnitude and an associated distortion profile, as defined in Equation 9.

$$w_{0,c}(x,y) = w_{0,c}^{\max} f_{0,c}(x,y) \tag{9}$$

The maximum distortion magnitude, $w_{0,c}^{\max}$, is prescribed by the ISSC, which provides the value given in Equation 10. The corresponding distortion profile, $f_{0,c}(x,y)$, is given in Equation 11.

$$w_{0,c}^{\max} = 0.0015\, a \tag{10}$$

$$f_{0,c}(x,y) = \sin\left(\frac{\pi x}{a}\right) \sin\left(\frac{\pi y}{b}\right) \tag{11}$$

When such column-type distortions occur in combination across a larger structural field, they result in what from now on is referred to as a global plate distortion. As with local distortions, global plate distortion can introduce additional secondary bending stresses, providing motivation for its inclusion in the present study.

2.2.3. Welded-joint geometries

The plate-to-support member geometries are typically connected through butt, T, and cruciform joints. Within these joint types, two common forms of misalignment are identified: linear misalignment and angular misalignment. Similar to initial out-of-plane plate distortions, both induce secondary bending stresses under loading. Studies by Mancini [29] and Lillemäe [30] have shown that such imperfections increase local stress concentrations at the weld, potentially reducing fatigue strength.

Imperfections related to weld geometry were investigated by Bartsch [31], who applied 3D laser scanning to quantify recurring weld imperfections and assess their influence on stress concentrations. The relevant imperfections and misalignments include excessive convexity, undercut, linear and angular misalignment, asymmetry of the fillet weld, and incorrect weld toe geometry.

Imperfections and misalignments associated with joint geometry, as well as deviations in the weld geometry itself, are not included within the present scope.

2.3. Overview

In modelling, a distinction is made between geometric parameters, global distortions, and local distortions. The only geometric parameter included is the shell plate thickness t_p, due to its strong influence on stiffness and stress. Out-of-plane plate distortions are represented by a global profile $w_{0,c}$ (column-type deflection) and a local profile $w_{0,pl}$ (deflection between adjacent stiffeners), both of which can induce secondary bending stresses under in-plane tensile loading. In addition, stiffener sideways distortion $w_{0,s}$ is included, as it can cause breathing effects in the web and further raise stresses at potential HS locations. Imperfections related to weld geometry, while known of influence [31], are excluded from the current scope. An overview of the selected imperfections are illustrated in Figure 4.

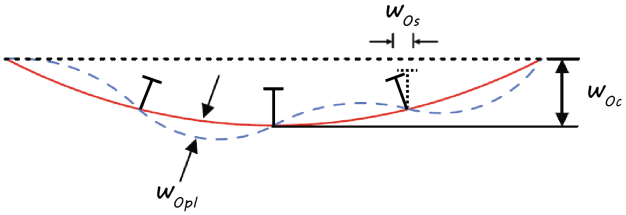

Figure 4: Overview of included distortions [24]

3. Probabilistic Framework

Developing a probabilistic framework requires a systematic reformulation of conventional deterministic methodologies into probabilistic representations. For the distortions under consideration, this involves translating their deterministic magnitudes into probability distribution functions. Ideally, such distributions are derived from high-fidelity measurements, such as those obtained via 3D laser scanning, capturing the actual as-built condition of structural components. In the absence of such data, however, literature-based measurements and fabrication tolerances specified by classification societies and design codes offer a viable alternative. The proposed framework therefore also facilitates a direct comparison between fatigue performance based on prescribed tolerances and that of actual as-built configurations.

3.1. Deterministic to Probabilistic

In the proposed framework the misalignments and imperfections are probabilistic by nature. As the actual distortion profiles might display local spatial variations, recent studies [15, 32] utilized random field theory to closely approximate uncertain initial distortions. A random field based approach complements classical probability theory, combining both methodologies allows to make the desired translation of deterministic to probabilistic.

3.1.1. Random Field Based Modelling

Based on the data of Ueda and Yao [19], Georgiadis [15] observed that regarding the local plate deflection the HH mode is dominant, but that local variations are present. The Stochastic Hungry-Horse (SHH) imperfection model was developed to capture local plate distortions within the HH mode, incorporating stochastic variations along the effective plate length. In the SHH model, these local variations are represented using the Spectral Representation Method (SRM), rooted in random field theory. The model has been validated for application in buckling analyses. To the authors' knowledge, however, the application of random field theory in the context of fatigue strength assessment remains largely unexplored.

The SHH model represents the deflection along the effective length, $w_{\text{eff}}(x)$, as the sum of a deterministic mean component w_0 and a zero-mean, homogeneous Gaussian random field $\tilde{f}(x)$, as shown in Equation 12 and illustrated in Figure 5. Realisations of this random field are generated using the SRM.

$$w_{\text{eff}}(x) = w_0 + \tilde{f}(x) \tag{12}$$

The full analytical local plate distortion profile is defined as:

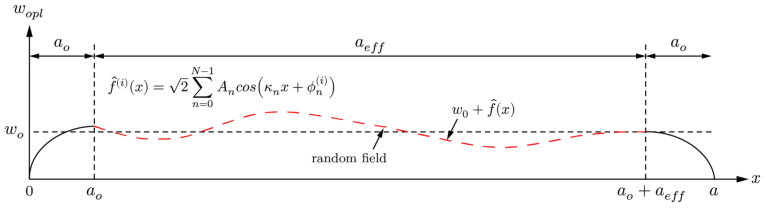

Figure 5: Stochastic Hungry Horse Model [26]

$$w_{0\text{pl}}(x,y) = \begin{cases} w_0 \left|\sin\left(\frac{\pi x}{2a_0}\right)\right| \sin\left(\frac{\pi y}{b}\right) & 0 \le x < x_0 \\ w_{\text{eff}}(x) \sin\left(\frac{\pi y}{b}\right) & a_0 \le x \le x_1 \\ w_0 \left|\sin\left(\frac{\pi(x-a_{\text{eff}})}{2a_0}\right)\right| \sin\left(\frac{\pi y}{b}\right) & x_1 \le x \le a \end{cases} \tag{13}$$

The Spectral Representation Method

Using the SRM, random field $\tilde{f}(x)$ is represented as a summation of N cosine terms, i.e. as a series expansion, with deterministic amplitudes and random phase angles. In general, any random field can be decomposed into a deterministic mean $\mu_X = \mathbb{E}[X(x)]$ and a zero-mean component $\tilde{f}(x)$, such that $\tilde{f}(x) = w_{\text{eff}}(x) - \mu_X$. A single realisation, representing one possible outcome of the random field, is generated using the series expansion given in Equation 14.

$$f^{(i)}(x) = \sqrt{2}\sum_{n=0}^{N-1} A_n \cos(\omega_n x + \phi_n^{(i)}) \tag{14}$$

$$A_n = \sqrt{2S(\omega_n)\Delta\omega} \tag{15a}$$
$$\omega_n = n\Delta\omega \tag{15b}$$
$$\Delta\omega = \frac{\omega_u}{N} \tag{15c}$$
$$A_0 = 0 \quad \text{or} \quad S(\omega_0) = 0 \tag{15d}$$

The amplitudes A_n are *deterministic* power spectral density dependent amplitudes and ϕ_n are random phase angles uniformly distributed in $[0,\ 2\pi]$. The cut-off frequency ω_u defines the upper-limit of the active region of the power spectral density function $S(\omega)$. The cut-off frequency is obtained using Equation 16 [15], where ϵ represents the fraction of ignored spectral density. It is typically denoted by a very small number in the order of $\mathcal{O} \sim 10^{-2}$ to 10^{-3}.

$$\int_0^{\omega_u} S(\omega)d\omega = (1-\epsilon)\int_0^{\infty} S(\omega)d\omega \tag{16}$$

The power spectral density $S(\omega)$ is associated with the autocorrelation function $R_f(\tau)$ proposed by Shinozuka and Deodatis [33], which ensures both boundedness and symmetry, as defined in Equation 17. In this formulation, l_c

denotes the correlation length and τ the lag, i.e. the relative spatial distance between two positions [34]. The correlation length represents the characteristic distance over which two points in the field remain significantly correlated before their statistical dependence becomes negligible.

$$R_f(\tau) = \sigma_f^2 \frac{l_c^2 \left(l_c^2 - 3|\tau|^2\right)}{(l_c^2 + |\tau|^2)^3} \tag{17}$$

The required spectral density formulation $S(\omega)$ is obtained by taking the Fourier transform of the autocorrelation function in equation 17, also known as the Wiener-Khintchine theorem. The resulting analytical formulation of the spectral density is defined in Equation 18, where σ_f denotes the variance of the measured field.

$$S(\omega) = \frac{\sigma_f^2}{4} l_c^3 \omega^2 \exp(-l_c|\omega|) \tag{18}$$

The length over which the SRM discretises the random field corresponds to the effective length of the plate field, a_{eff}. Both the effective length and the correlation length are expressed as functions of the aspect ratio, as defined in Equations 19, 20, and 21 [19, 34].

$$a_{\text{eff}} = a - 2a_0 \tag{19}$$

$$\frac{l_c}{a} = \begin{cases} 0.208, & \text{if} \quad \sqrt{2} \le a/b < \sqrt{6} \\ 0.277, & \text{if} \quad \sqrt{6} \le a/b < \sqrt{12} \\ 0.311, & \text{if} \quad \sqrt{12} \le a/b < \sqrt{20} \\ 0.332, & \text{if} \quad \sqrt{20} \le a/b < \sqrt{32} \end{cases} \tag{20}$$

$$a_0 = \begin{cases} a/4 & \text{if} \quad \sqrt{2} \le a/b < \sqrt{6} \\ a/6 & \text{if} \quad \sqrt{6} \le a/b < \sqrt{12} \\ a/8 & \text{if} \quad \sqrt{12} \le a/b < \sqrt{20} \\ a/10 & \text{if} \quad \sqrt{20} \le a/b < \sqrt{32} \end{cases} \tag{21}$$

Ideally, the correlation length is determined by minimising the root mean square error between the proposed autocorrelation function in Equation 17 and a polynomial fit of the spatial autocorrelation of the measured deflections, as defined in Equation 22, where d denotes the measured deflections and μ and σ represent the first and second statistical moments of the measured plate field, respectively.

$$\hat{\rho}_d(\tau) = \frac{1}{n-1} \sum_{i=1}^{n} \frac{(d_{x_i} - \mu)(d_{x_{i+\tau}} - \mu)}{\sigma^2} \tag{22}$$

3.1.2. Random Variable-Based Modelling

For the remaining identified imperfections, namely plate thickness, global plate distortion, and stiffener sideways distortion, no measurement datasets are available to substantiate local spatial variations in their deflection profiles. Therefore, a random variable based approach is adopted.

The analytical profile functions defined earlier describe the shape of each imperfection along the element length. Uncertainty is introduced by treating their maximum amplitudes as normally distributed random variables:

$$\begin{aligned} w_{0,\text{c}}(x,y) = w_{0,c}^{\max} f_{0,c}(x,y) \quad &\rightarrow \quad w_{0,\text{c}}^{\max} \sim \mathcal{N}(\mu, \sigma^2) \\ w_{0,\text{s}}(x,z) = w_{0,\text{s}}^{\max} f_{0,\text{s}}(x,z) \quad &\rightarrow \quad w_{0,\text{s}}^{\max} \sim \mathcal{N}(\mu, \sigma^2) \end{aligned}$$

Since steel plates are hot rolled, the plate thickness t_p is assumed uniform across the plate:

$$t_p \sim \mathcal{N}(\mu, \sigma^2)$$

In the absence of comprehensive measurement data, the normal distribution provides a mathematically convenient and widely accepted first approximation for representing uncertainty. If future measurements confirm local spatial variability for these imperfections, the present random variable formulation can be extended to a random field representation using the SRM.

This approach allows efficient uncertainty propagation in numerical simulations and complements the random field based models used for local imperfections, enabling a comprehensive probabilistic framework that represents the initial distortions.

3.2. Bayesian Inference

A probabilistic approach requires large data sets. However, measurements of imperfections and misalignments in maritime structures are scarce and may only become available over time. Once new observations are obtained, they can be incorporated with prior knowledge to refine estimations. This process follows the Bayesian Inference framework, which systematically updates prior beliefs as new data becomes available removing the uncertainty present in prior beliefs.

When a new set of measured data points $(x_1, x_2, \ldots, x_n)$ becomes available. The *likelihood* $\mathcal{L}$ of observing these data points, given the hyper-parameter θ, is the joint probability of the individual observations under the assumption of independence. It is computed as the product of $f_X(x_i \mid \theta)$ evaluated at all data points, as defined in equation 23 [35, 36].

This posterior distribution represents the updated knowledge of θ after incorporating the new data, thereby reducing the uncertainty in model parameters and improving the accuracy of probabilistic fatigue assessment.

$$\mathcal{L}(\theta) = \prod_{i=1}^{n} f_X(x_i|\theta) \tag{23}$$

The posterior function, denoted by $f''(\theta)$, of the hyper-parameters is then obtained similarly to Bayes' theorem using equation 24, in which k is a normalizing constant.

$$f''(\theta) = k\mathcal{L}(\theta)f'(\theta) \tag{24}$$

$$k = \left[\int_{-\infty}^{+\infty} \mathcal{L}(\theta)f'(\theta)\,d\theta\right]^{-1} \tag{25}$$

Bayesian inference is particularly valuable when only a few high-fidelity measurements are available (e.g., 3D scan data). It enables robust probabilistic modelling by continuously refining distributions without requiring large datasets from the outset.

Within the current framework, the input consists of probability distributions of imperfections and misalignments, and the output consists of SCF distributions. The update is therefore recommended to be applied to the input distribution functions to maintain causality between the increasingly certain inputs and the resulting SCFs. This preserves the physical link between fabrication variability and structural response and ensures that the input distributions remain applicable to different geometries and loading scenarios.

3.3. Halton Sequences

To evaluate the influence of misalignments and imperfections a substantial amount of combinations must be simulated. A key challenge arises in the fact that the required number of simulations increases exponentially with both the number of misalignments as well as the discretization points of each individual misalignment or imperfection.

To avoid full factorial sampling, Halton Sequences are utilized to generate sample points that are uniformly distributed across a multidimensional space. Halton sequences are deterministic low-discrepancy sequences where dimension is associated with a distinct prime number base, and sample values are constructed using the radical inverse function in that base. This structure ensures that points are distributed more evenly than with purely random sampling [37, 38].

Consider the first elements of a Halton sequence in base 2 and base 3. In base 2, the interval $[0, 1]$ is divided into halves, fourths, eighths, and so on. Similarly, in base 3, the interval is divided into thirds, ninths, twenty-sevenths, and so on. Figure 6 demonstrates the space-filling property of a 2D Halton sequence for $N = 1000$ samples.

Base 2: $\frac{1}{2}, \frac{1}{4}, \frac{3}{4}, \frac{1}{8}, \frac{5}{8}, \frac{3}{8}, \frac{7}{8}, \cdots$

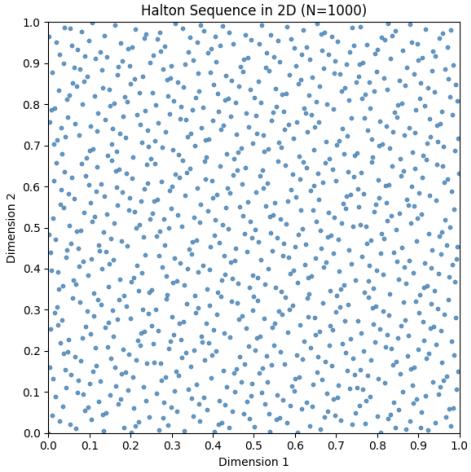

Figure 6: Halton Sequence in 2D

Base 3: $\frac{1}{3}, \frac{2}{3}, \frac{1}{9}, \frac{4}{9}, \frac{7}{9}, \frac{2}{9}, \frac{5}{9}, \cdots$

While Halton sequences provide good space-filling properties in low dimensions, they may perform less in higher dimensions due to closely spaced prime bases. In higher dimensions it is recommended to make use of the scrambled Halton Sequence.

3.4. Framework Overview

The previously described methods are integrated into a comprehensive probabilistic fatigue assessment framework, as illustrated in Figure 7. The framework facilitates the evaluation of geometric imperfections and misalignments on the fatigue strength of (arc-)welded maritime structures, by linking stochastic modelling techniques with finite element analysis. The key steps of the framework are defined as follows:

1. **Definition of Distortion Profiles and PDFs**
   The relevant geometric imperfections and misalignments are identified and analytically described. Each imperfection is assigned a distortion profile based on physical assumptions, validated models or measured data. From statistical analysis the relevant statistical moments and distributions are obtained.

2. **Stochastic Sample Generation**
   A large number of statistically independent input samples are generated. For imperfections modelled via random fields, realizations are constructed using the Spectral Representation Method. For scalar random variables, values are sampled using a **Halton sequence**, ensuring uniform coverage of the high-dimensional parameter space. If measurement data becomes available during or after this step, **Bayesian inference** is applied to update the assumed distributions. This enables the framework to refine the input space in light of new observations, ensuring that the generated samples remain consistent with both prior

knowledge and observed as-built variability.

3. **Finite Element Model Assembly**
   A parametric finite element model of a representative stiffened panel is assembled using `PyMAPDL`, which enables efficient use of coded functions and loops to systematically evaluate different combinations of imperfections and misalignments. Sampled imperfections are embedded directly into the model geometry by defining keypoint positions.

4. **Application of Loads and Boundary Conditions**
   The structure is subjected to two distinct loading cases: global hull girder bending (GHGB) and water pressure (WP), with boundary conditions defined according to the specific geometry.

5. **Structural Stress Evaluation at Hot Spots**
   Nodal forces and moments from the finite element model are used to extract HS structural stresses at fatigue relevant details. Three assessment methods are used:
   - *Type A*: Extension of the virtual node method [39]
   - *Type B*: Local notch-affected zone assessment using an artificial plate thickness t_p'
   - *Type C*: Structural stress evaluation along weld paths based on Dong's matrix formulation [40]

6. **Post-Processing and Statistical Evaluation**
   SCFs are computed by normalizing local HS stresses with respect to a reference stresses. The resulting SCF distributions quantify the influence of geometric uncertainty on fatigue critical stress response and can be used to inform tolerance development and design margins.

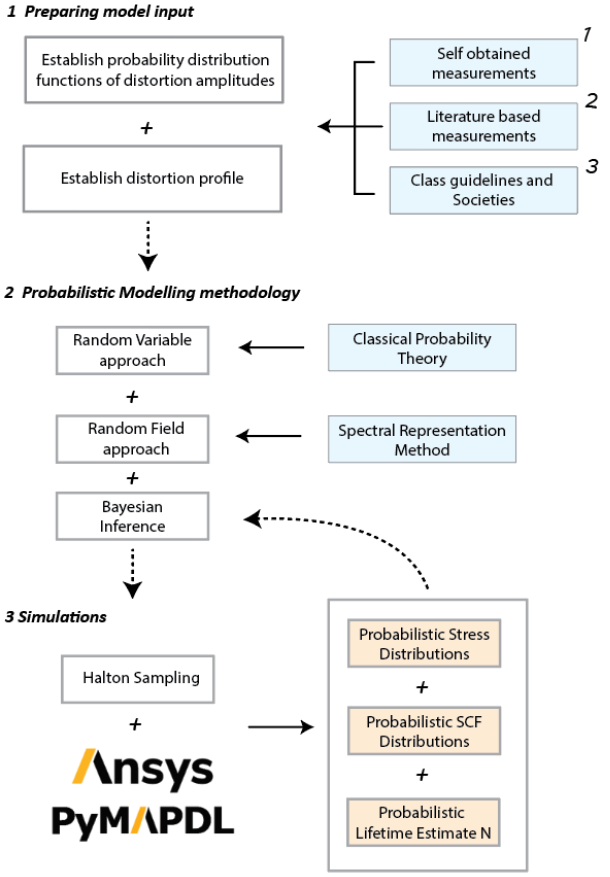

Figure 7: Overview of the proposed probabilistic framework

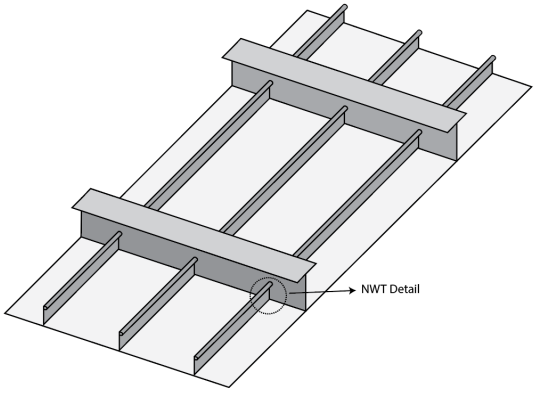

Figure 8: Stiffened Panel Configuration

4. Benchmark Study

The proposed probabilistic framework, which models initial distortions using a combination of random variables and random fields, is theoretically applicable to any structural configuration. To evaluate its applicability, a benchmark case study is conducted in which all theoretical components and procedural steps outlined in Figure 7 are integrated.

4.1. Stiffened Panel Geometry

The benchmark case study is conducted on a classical stiffened panel configuration. This configuration, comprising two transverse frames and three longitudinal stiffeners, is representative of a typical structural panel found in highly loaded regions of the bottom hull amidships. The geometric layout is shown in Figure 8, with key dimensions and parameters illustrated in Figure 9 and summarised in Table 1. Symmetry conditions are present along all outer edges of this panel.

The longitudinal stiffeners in the study are bulb (HP) stiffener profiles, while the transversal frames are T-stiffener profiles. The longitudinal bulb stiffeners are continuous over the length, penetrating the transversal T-stiffeners with the Non-Watertight connection detail illustrated in figure 10.

The selected stiffened panel geometry was chosen because it represents panels found in highly loaded hull regions, where fatigue-critical connections frequently occur. It includes the Non-Watertight (NWT) connection detail,

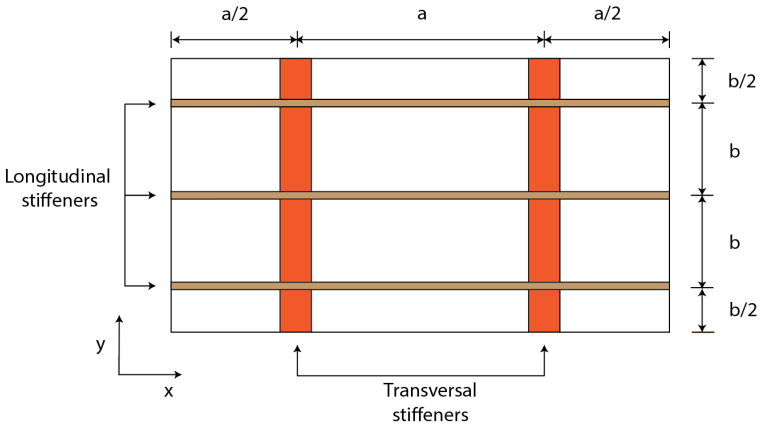

Figure 9: Layout Stiffened Panel Configuration

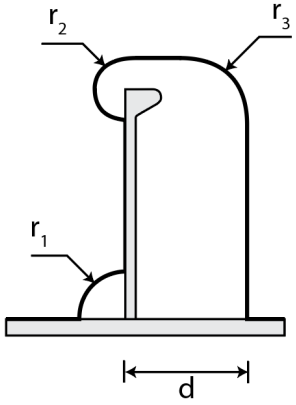

Figure 10: Non-Watertight (NWT) cutout detail

Table 1
Geometric and material properties of the assembly

Parameter	Description	Value
Plate Properties		
a	Length of a bay	3.44 m
b	Width of a bay	0.78 m
t_p	Plate thickness	0.011 m
Longitudinal Stiffener (HP 200×10)		
$h_{w,\text{long}}$	Web height	0.200 m
$t_{w,\text{long}}$	Web thickness	0.010 m
$b_{f,\text{long}}$	Flange width (equivalent)	0.033 m
$t_{f,\text{long}}$	Flange thickness (equivalent)	0.020 m
Transversal Stiffener (T-profile)		
$h_{w,\text{trans}}$	Web height	0.400 m
$t_{w,\text{trans}}$	Web thickness	0.010 m
$b_{f,\text{trans}}$	Flange width	0.150 m
$t_{f,\text{trans}}$	Flange thickness	0.012 m
NWT Cutout		
r_1	Radius Mouse Hole (MH)	0.044 m
r_2	Upper smaller radius	0.020 m
r_3	Upper larger radius	0.035 m
d	Frame-bulb spacing	0.071 m
Fillet weld		
l_w	Leg length	0.006 m
Material Properties (Steel)		
E	Young's modulus	$210 \cdot 10^9$ N/m^2
ν	Poisson's ratio	0.3 [-]
ρ	Density	7800 kg/m^3

intersecting stiffeners, and plating, which together capture the main features influencing the interaction between imperfections and stress concentrations. This makes it a realistic and relevant case for evaluating the probabilistic framework.

Assumptions

The benchmark case study presented in this section are based on the following assumptions:

(i) Welding is performed using the arc-welding method, where the welding parameters including current, voltage, speed and heat input are constant

(ii) The assumed welding sequence of the configuration is:
  (a) Longitudinal bulbs are positioned on the plates at their ideal positions
  (b) Frames are positioned over the bulbs at their ideal positions
  (c) The bulbs and frames are temporarily connected by tack welds
  (d) The longitudinal bulbs are welded to the plates
  (e) The transversal frames are welded to the plates
  (f) At last, the NWT detail connections are arc-welded

(iii) The twelve plate fields are modelled as as single plate to avoid the presence of butt welds

(iv) Because the bulb-frame connections are tack welded, clamped-clamped boundary conditions are assumed to correspond to the initial stiffener sideways distortion profile

(v) The longitudinal bulb stiffeners are modelled as an angle bar stiffener with an equivalent flange width and thickness so the moments of inertia match

(vi) Webs of distorted stiffener profiles remain ideally straight over the web height

(vii) Flanges of distorted stiffener profiles remain perpendicular to the stiffener web

(viii) As the assembly resembles a bigger configuration. The transversal frames are assumed to be three times as long. The sideways distortion of the frames is modelled as the middle third part of a half sine wave

(ix) Residual stresses resulting from the welding process are omitted

4.2. Benchmark Study: Probabilistic Representation

To define the necessary input for the simulation framework, both the distortion profiles and the associated probability distribution functions are established. While the most robust approach would involve high-fidelity measurements of the entire structure, such as 3D laser scanning followed by statistical analysis, the present benchmark case study is based on a solid foundation of publicly available datasets and fabrication tolerances provided by classification society guidelines and standards.

Due to the lack of representative data, both global plate distortions and plate thickness variations are excluded from the present benchmark study. Nevertheless, these features have been implemented in the FE simulation framework, allowing for their inclusion in future analyses with minimal additional effort.

4.2.1. Local Plate distortion

The SRM, as previously introduced, allows the generation of random fields with a prescribed correlation structure. This is based on a specified spatial autocorrelation function and the standard deviation of an observed field. In the present study, input data are taken from experimental measurements reported by Ueda and Yao [19]. These measurements, shown in Figure 11, were obtained from six plate fields with dimensions $3440 \times 780 \times 11$ mm, which are adopted in this benchmark case study. Visible in Figure 11, the dominant deformation profile corresponds to the HH mode, while local variations are evident along the effective plate length, substantiating the statement statement made before.

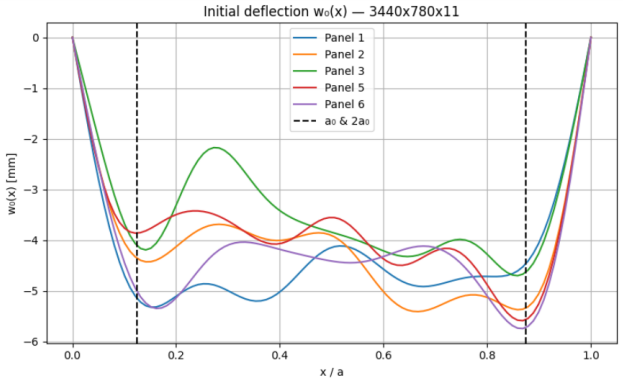

Figure 11: Profiles derived from the amplitudes presented by Ueda and Yao [19]

Based on the measured deflection profiles and corresponding spatial correlation, the SRM is employed to generate sample functions, e.g. realizations. As an illustration, a total of $N = 1000$ realisations are produced. Statistical comparison between the measured data and the realization of the SRM confirms the robustness of the method. As shown in Figure 12, the generated fields exhibit closely-matching first- and second-order statistical moments, demonstrating that the correlation structure and variance are accurately preserved.

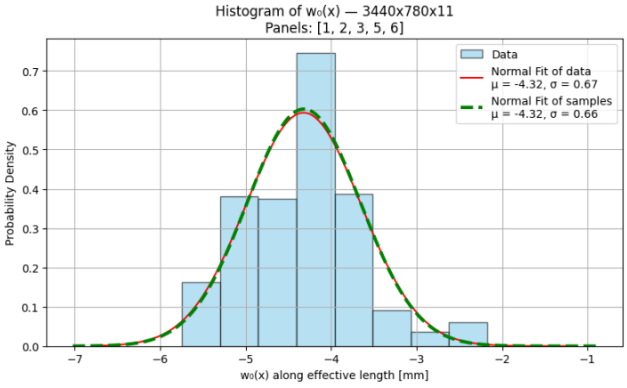

Figure 12: SRM realizations versus measurements

In the FE simulation framework, each simulation prescribes twelve new SRM realizations to each plate individually, with each plate field treated as statistically independent. The realizations are defined in PyMAPDL as splines using the SHH formulation defined in equation 13.

4.2.2. Stiffener Sideways Distortion

In the absence of representative measurement data on sideways distortions of continuous stiffeners, both longitudinal and transverse, the tolerances specified in IACS No. 47 are adopted as the initial estimate for maximum distortion amplitudes. Two ranges are defined: a *Standard* range, which reflects the deviations expected to occur under normal fabrication conditions, and a *Limit* range, which specifies the maximum allowable deviation beyond the Standard range.

The prescribed Standard tolerance corresponds to ± 1 mm per metre length of the structural member, and the Limit tolerance to ± 2.5 mm. By assuming that the maximum allowable distortions correspond to $\pm 2\sigma$ of the respective probability density functions, normal distributions can be defined to represent the distortions. It should be noted that, although the bulb stiffener is continuous over the full length, distortions occur locally between adjacent frames, i.e., over the length of a single bay. The resulting normal distribution parameters for both longitudinal and transversal stiffener distortions are summarised in Table 2.

Table 2
Normal distributions of $f_{0,s}^{\max}$ corresponding to the IACS No. 47 *Standard* range

Stiffener profile	Length	$\mathcal{N}(\mu, \sigma^2)$ [mm]
Longitudinal bulb stiffener	a	$\mathcal{N}(0, 1.72^2)$
Transversal T-stiffener	$9b$	$\mathcal{N}(0, 3.51^2)$

Assuming the longitudinal bulb stiffeners are tack-welded to the transversal frames prior to final welding, their distortion shape is approximated using the mode shape derived from clamped–clamped boundary conditions. The profile is first normalised and subsequently scaled by the normally distributed maximum amplitude:

$$\hat{\Psi}(x) = \frac{\Psi(x)}{\max|\Psi(x)|} \tag{26}$$

$$w_{0,\mathrm{s,\ long}}(x) = w^{\max}_{0,\mathrm{s,long}}\hat{\Psi}(x) \quad \rightarrow w^{\max}_{0,\mathrm{s,long}} \sim \mathcal{N}(\mu_s, \sigma_s^2) \tag{27}$$

For the transversal T-stiffeners, a simply-supported mode shape is adopted where the central third of a half-sine wave is modelled.

4.2.3. Halton Samples

The structural configuration includes 12 plate fields, with distortions in the nine longitudinal stiffener segments and two transverse frames represented by 11 independent, normally distributed random variables. In each simulation, plate field distortions are generated separately using the SRM, while the Halton sequence samples the stiffener and frame distortion amplitudes within bounds of ± 2 standard deviations, covering approximately 95.4% of the probability density. It was verified that the generated samples adequately cover the intended sample space.

4.3. Finite Element Simulations

With the probability distributions and distortion profiles established, the required input for the finite element simulations was prepared. The benchmark study was conducted for two loading conditions: (1) hydrostatic water pressure (WP), and (2) global hull girder bending (GHGB), the latter approximated by a membrane stress component. For both load cases, five distinct simulation cases were analysed:

1. Idealised geometry without imperfections
2. Including local plate distortion only
3. Including longitudinal bulb distortion only
4. Including transversal frame distortion only
5. Including all imperfections simultaneously

This approach serves not only to evaluate the performance of the simulation framework, but also to gain insight into the individual contribution of each imperfection type on the local structural stress response.

4.3.1. Loading- and Boundary Conditions

Figure 9 illustrates the stiffened panel assembly, which applies symmetry boundary conditions on all four edges to simulate continuity with the surrounding structure. The boundary conditions are selected to realistically approximate the structural response under both loading conditions.

Under water pressure loading, symmetry is enforced on all edges, and vertical translation (u_z) is restricted at the bottom edges of the transverse frames. In the case of GHGB, the same symmetry conditions are maintained; however, an additional constraint is introduced in the longitudinal direction (u_x) on one side to prevent rigid-body motion under axial tensile loading. The complete set of boundary conditions for both load cases is summarised in Table 3.

Table 3
Boundary conditions for Water Pressure (WP) and Global Hull Girder Bending (GHGB), corresponding to Figure 9

Location	Direction	Constraint
Water Pressure:		
$x = 0,\ x = 2a$	$u_x,\ \varphi_y$	0
Global Hull Girder Bending:		
$x = 0$	$u_x,\ \varphi_y$	0
Both Load Cases:		
$y = 0,\ y = 3b$	$u_y,\ \varphi_x$	0
$x = \frac{a}{2},\ y = 0,\ z = 0$	u_z	0
$x = \frac{3a}{2},\ y = 0,\ z = 0$	u_z	0
$x = \frac{a}{2},\ y = 3b,\ z = 0$	u_z	0
$x = \frac{3a}{2},\ y = 3b,\ z = 0$	u_z	0

Both loading cases are subjected to a unit load of 1 $\mathrm{N/mm^2}$ (or 1 MPa), as the objective is to evaluate the relative influence of geometric distortions on the stress distribution, rather than to assess in-service loading conditions.

In the WP load case, the pressure is applied as a surface load on all elements located at the bottom face of the panel. For the GHGB case, the load is implemented by applying a nodal force through a master–slave node relationship at the unconstrained longitudinal edge of the panel, ensuring a uniform membrane stress field representative of a unit load hull girder bending stress.

4.3.2. Fatigue Assessment

The NWT detail used in this study presents several considerations relevant to fatigue assessment. The structural behaviour of this detail is primarily governed by shear stresses, as it facilitates the transfer of loads from the longitudinal bulb stiffener to the transversal frames. Notably, the absence of a collar plate implies that the load transfer occurs entirely through the single side of the connection. A total of four potential HS locations at the NWT detail are identified where fatigue-critical stress concentrations may develop, as illustrated in Figure 13:

i. The upper notch of the bulb-to-frame connection,
ii. The lower notch of the bulb-to-frame connection,
iii. The lower notch of the MH of the frame-to-plate connection,
iv. The lower notch of the cutout of the frame-to-plate connection.

Each simulation the `PyMAPDL` framework assesses all four potential HS locations, as the governing location may shift depending on the specific distortion combination introduced in the model. Depending on the direction of the assumed crack path two types of HS's are assessed; type A and B. Additionally, HS type C is assessed along the transverse frame–plate connection at $x = \frac{a}{2}$ and $x = \frac{3a}{2}$ in Figure 9, hereafter denoted as type $\mathrm{C_{FP}}$, as well as at the NWT detail along the weld between locations *i* and *ii*, hereafter denoted

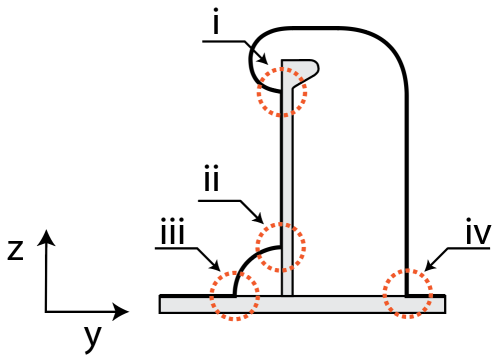

Figure 13: Four potential Hot Spot locations

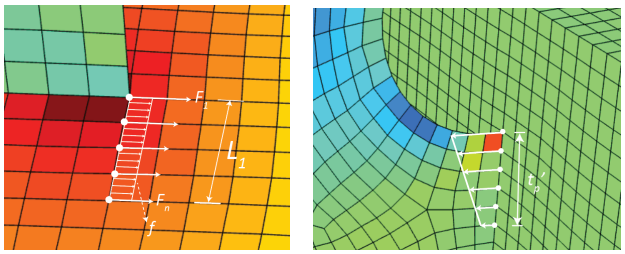

(a) HS Type A σ_s extraction (b) HS Type B σ_s extraction

Figure 14: HS Structural stress σ_s extraction methods

as type C_{NWT}.

Within displacement-based finite element formulations, the most reliable results are typically the nodal displacements and nodal forces, as equilibrium is explicitly satisfied at nodal locations. Consequently, as shell elements are used in this benchmark study, nodal forces are utilized to extract structural stresses at the HS locations [39].

Structural Stress Extraction - HS Type A

The Hot Spot Type A assessment is based on the virtual node method proposed by Dong [39], which redistributes nodal forces into a line force acting over the plate thickness of the connection plate, including the weld seam, denoted as L_1. This redistribution is only valid if the element size is sufficiently large. However, when modelling misalignments and distortions, a fine mesh is required to accurately capture geometric variations and to avoid triangulation in the regions of interest. As a result, the original virtual node method becomes inapplicable.

To address this limitation, the nodal forces acting over L_1 are averaged and redistributed into an equivalent line force f, as illustrated in Figure 14(a). The effective length L_1 is defined in Equation 28, where t_c denotes the thickness of the *connection* plate. Both the equivalent line force and the corresponding moment are obtained through this averaging procedure. The structural stress components are subsequently determined using Equation 29, where t_b is the thickness of the *base* plate, and f_n and m_n represent the nodal forces and moments in the relevant directions. The structural HS stress is evaluated on both sides of the connection plate.

$$L_1 = \frac{t_c}{2} + l_w, \quad f_n = \frac{\sum F_n}{L_1} \tag{28}$$

$$\sigma_{s,m} = \frac{f_n}{t_b}, \qquad \sigma_{s,b} = \frac{6m_n}{t_b^2} \tag{29}$$

Structural Stress Extraction – HS Type B

In a Hot Spot Type B assessment, illustrated in Figure 14(b), the membrane- and bending components $\sigma_{s,m}$ and $\sigma_{s,b}$ are determined over an artificial plate thickness t'_p, denoting the notch-affected zone. The notch-affected zone is typically taken as a fraction of the actual plate thickness, ranging from $0.1t_p$ to $0.2t_p$, with a typical value of 20 *mm*.

Similar to a type A assessment, the nodal forces acting over t'_p are redistributed into an equivalent line force after which the membrane and bending components are obtained using equations 30 and 31, where n denotes the relevant direction.

$$\sigma_{s,m} = \frac{\sum f_{n,i}}{t'_p}, \quad f_{y,i} = \frac{F_{n,i}}{t_p} \tag{30}$$

$$\sigma_{s,b} = \frac{6\left(\sum f_{y,i} \cdot x_i - \sigma_{s,m} \cdot \frac{t'^2_p}{2}\right)}{t'^2_p} \tag{31}$$

Structural Stress Extraction – HS Type C

The HS Type C assessment follows the structural stress recovery procedure proposed by Dong [39]. Structural stresses along a weld line are obtained through interpolation of nodal forces and moments using an element size dependent interpolation matrix $[L]$, which for an open weld path takes the following matrix form:

$$[F] = [L][f]$$

$$\begin{Bmatrix} F_1 \\ F_2 \\ F_3 \\ \vdots \\ F_n \end{Bmatrix} = \begin{bmatrix} \frac{l_1}{3} & \frac{l_1}{6} & 0 & \cdots & 0 \\ \frac{l_1}{6} & \frac{l_1+l_2}{3} & \frac{l_2}{6} & \ddots & \vdots \\ 0 & \frac{l_2}{6} & \frac{l_2+l_3}{3} & \ddots & 0 \\ \vdots & \ddots & \ddots & \ddots & \frac{l_{n-1}}{6} \\ 0 & \cdots & 0 & \frac{l_{n-1}}{6} & \frac{l_1}{3} \end{bmatrix} \begin{Bmatrix} f_1 \\ f_2 \\ f_3 \\ \vdots \\ f_n \end{Bmatrix} \tag{32}$$

Solving this for both the nodal force vector $[F]$ and the nodal moment vector $[M]$, the membrane and bending stress vectors are determined as:

$$[\sigma_m] = \frac{1}{t}[f] \qquad [\sigma_b] = \frac{1}{t^2/6}[m] \tag{33}$$

Reference Stresses

As the SCFs denote the magnitude of the HS stress with respect to the reference stress, the reference stresses are required. The reference stress of the WP loading case is determined using beam mechanics, and that of the GHGB case is equal to the applied tensile stress of 1 N/mm^2.

Mesh Convergence

As mentioned, a fine mesh is required to avoid triangulation near HS locations. A mesh convergence study is performed on the four previously mentioned HS locations. Illustratively, the mesh convergence of cutout 2 is shown in table 4. In the final simulations, a mesh size of 0.003 is used around the locations of the cutouts and of 0.006 in the remaining areas.

Table 4
Mesh Convergence of Detail 2 of HS Type B under WP loading

HS Location	0.005 [m]	0.004 [m]	0.003 [m]
I	-0.751	-0.710	-0.673
II	0.492	0.464	0.443
III	0.518	0.502	0.486
IV	0.485	0.471	0.463

4.4. Results

Incorporating the structural stress extraction methods within the PyMAPDL simulation framework results in 72 Type A and B evaluations and 1562 Type C evaluations per simulation and loading condition. This section presents the governing HS results for the previously defined geometric imperfection cases and loading scenarios. The tables provide the governing HS distributions with reference to the locations specified in Section 4.3.2. Due to space limitations, only the governing distributions are included here; the complete set of results is available upon request.

4.5. Effect of Local Plate Distortions

The first simulation set isolates the influence of local plate distortions as described by the SHH, excluding other imperfection types and global misalignments. This is the only simulation set directly based on measurement data. SCFs of the governing HS for both loading conditions, together with the SCF of the idealised geometry, are summarised in Table 5.

In all cases, the presence of local plate distortion leads to deviations in SCF values. Under WP loading, a *reduction* in mean SCF is observed at all assessed locations relative to the idealised geometry. In contrast, all HS type C locations under GHGB show a relative increase in SCF, whereas HS type A and B locations exhibit both modest increases and reductions. Results and corresponding SCF distributions for the governing HSs under WP and GHGB loading are shown in Figures 15 and 16.

Table 5
SCFs of the governing Hot Spot due to w_{0pl} only

HS	Detail	Location	$\mathcal{N}(\mu_{SCF}, \sigma^2_{SCF})$	SCF^{ideal}
Water Pressure				
A	1	IV : b	$\mathcal{N}(1.30, 0.061^2)$	2.24
B	1	IV	$\mathcal{N}(0.52, 0.027^2)$	0.93
C_{NWT}	6	$z \approx 0.1$ [m]	$\mathcal{N}(0.98, 0.058^2)$	−0.49
C_{FP}	-	$x = \frac{a}{2}$, $y \approx 0.28$ [m]	$\mathcal{N}(1.63, 0.074^2)$	2.84
Global Hull Girder Bending				
A	1	IV : b	$\mathcal{N}(0.29, 0.011^2)$	0.37
B	6	I	$\mathcal{N}(0.11, 0.018^2)$	0.07
C_{NWT}	2	$z \approx 0.1$ [m]	$\mathcal{N}(1.30, 0.023^2)$	0.90
C_{FP}	-	$x = \frac{1.5a}{2}$, $y \approx 2.30$ [m]	$\mathcal{N}(1.92, 0.105^2)$	1.03

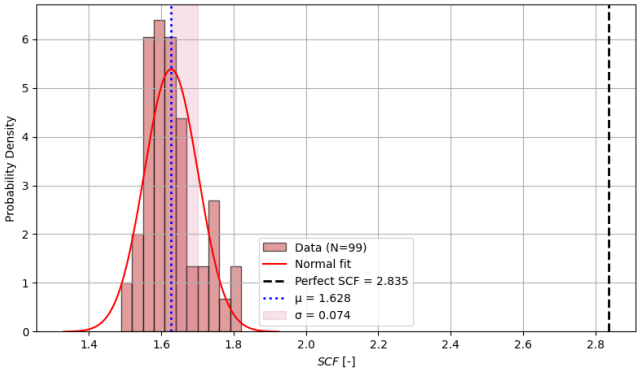

Figure 15: Governing SCF distribution for local WP and w_{0pl} only

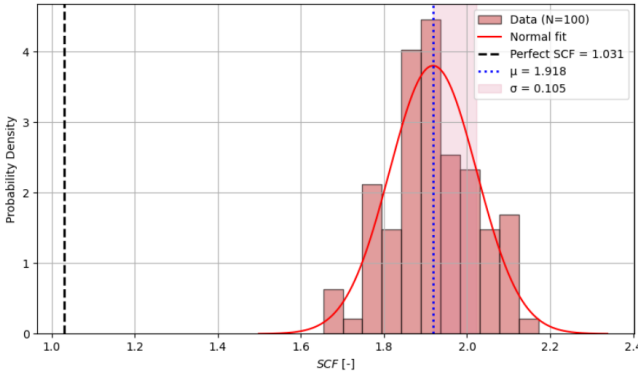

Figure 16: Governing SCF distribution for GHGB and w_{0pl} only

4.5.1. SCF Reduction in WP loading

Ideally straight plates primarily resist WP loading through bending. The introduction of initial out-of-plane distortions in the SHH profile alters the load transfer mechanism by redistributing part of the applied load into in-plane membrane stresses. Since the bending stiffness of a plate scales cubically with plate thickness ($\sim Et_p^3$), whereas the membrane stiffness scales linearly ($\sim Et_p$), in-plane membrane strain requires more energy in thin plates, providing a stiffer

response than pure bending. The distorted panels modelled using the SHH therefore exhibit a higher effective stiffness under WP loading than the idealised geometry.

To verify this effect, a dedicated FE simulation was performed on a single plate field with same dimensions as in the benchmark study and clamped–clamped boundary conditions along all edges. In this simulation the distortion amplitude was gradually increased from zero (ideal plate) to a full realization of the SHH plate field. Figure 17 presents the mid-plate deflection along the span for each imperfection amplitude. The results show that increasing distortion amplitude reduces the overall deflection, demonstrating that the panel response is more stiff than the idealized plate under WP loading. This mechanism contributes directly to the observed reduction in mean SCF.

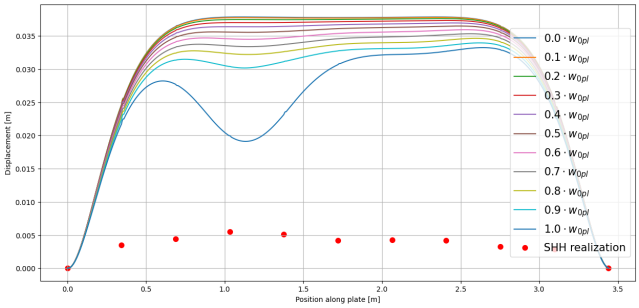

Figure 17: Mid plate deflection for increasing SHH distortion

Examining the stress contributions of the governing type C_{FP} HS in Figure 18 shows that the bending stress component in the imperfect geometry is significantly reduced relative to the idealised case, while the membrane stress component becomes more tensile. These observations are consistent with the previously stated explanation.

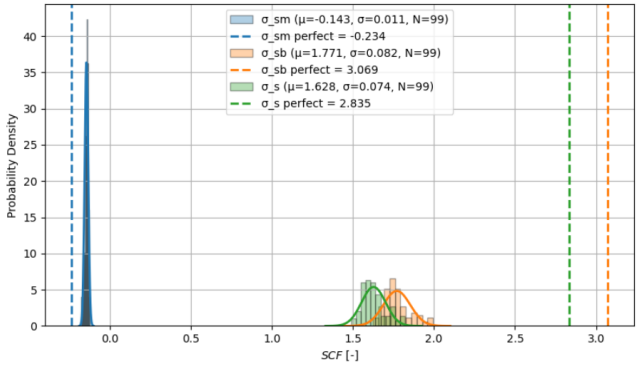

Figure 18: Membrane-, bending- and structural stress components of governing HS Type C_{FP} in WP loading

4.5.2. SCF increase in GHGB loading

When subjected to GHGB loading, tensile in-plane membrane stresses cause a straightening effect on initially out-of-plane distorted plates, inducing secondary bending moments that elevate local stress levels and increase SCF values. This mechanism is supported by the stress decomposition at the governing type C_{FP} HS, as illustrated in Figure 19. In the idealised geometry, the structural stress is dominated by the membrane component. In contrast, for imperfect geometries the observed increase in total structural stress arises predominantly from an increase in the bending stress component, leading to an SCF almost twice as high, aligning with physical expectations.

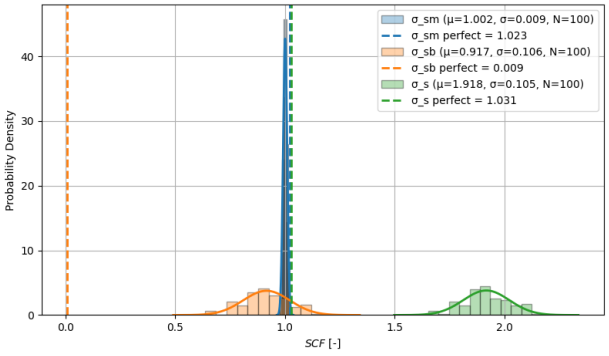

Figure 19: Membrane-, bending- and structural stress components of governing HS Type C_{FP} in GHGB loading

4.6. Effect of Longitudinal Bulb Distortion

The second simulation set isolates the influence of longitudinal bulb stiffener distortions, modelled using the first mode shape for clamped–clamped boundary conditions. Distortion amplitudes were sampled from normal distributions corresponding to the *Standard* range defined in IACS No. 47. Across both WP and GHGB loading, the results showed only minor deviations from the SCFs of the idealised geometry, indicating that under the present assumptions these distortions exert negligible influence on the local stress response. To further explore modelling sensitivity, additional simulations were carried out with amplitudes corresponding to the *Limit* range of IACS No. 47 to assess the effect of distortion magnitude, and with simply supported shapes to evaluate the role of boundary conditions.

The simply supported and clamped–clamped mode shapes produced comparable results in GHGB, with mean SCFs remaining close to the idealised values. Both shapes, however, showed noticeable variability at HS Type C of the NWT details, suggesting that the influence of bulb stiffener distortions is governed primarily by distortion magnitude rather than by the assumed mode shape.

The resulting SCFs for the governing HSs under both loading conditions for the clamped–clamped case, together with those of the idealised geometry, are presented in Table 6. For consistency with the adopted assumptions, and since SCF variability was similar across both distortion shapes and loading conditions, the clamped–clamped shape

with amplitudes corresponding to the *Limit* range is applied in the remainder of the study.

Table 6
Results of the governing Hot Spot for $f_{0,s}^{\text{long}}$ only

HS	Detail	Location	$\mathcal{N}(\mu_{SCF}, \sigma^2_{SCF})$	SCF$^{\text{ideal}}$
Water Pressure				
A	4	IV : b	$\mathcal{N}(2.24, 0.000^2)$	2.24
B	1	IV	$\mathcal{N}(0.93, 0.000^2)$	0.93
C_{NWT}	4	$z \approx 0.15$ m	$\mathcal{N}(1.97, 0.031^2)$	1.97
C_{FP}		$x = \frac{a}{2}$, $y \approx 1.1$ [m]	$\mathcal{N}(1.25, 0.002^2)$	2.84
Global Hull Girder Bending				
A	6	IV : b	$\mathcal{N}(0.37, 0.004^2)$	0.37
B	3	II	$\mathcal{N}(0.08, 0.001^2)$	0.08
C_{NWT}	3	$z \approx 0.15$ m	$\mathcal{N}(1.52, 0.149^2)$	1.52
C_{FP}	-	$x = \frac{a}{2}$, $y \approx 0.20$ [m]	$\mathcal{N}(1.02, 0.003^2)$	1.02

The imperfect scenarios show negligible influence at HS Types A and B, which are attributed to the assumed boundary conditions. In the present model, longitudinal stiffener distortions are represented by clamped–clamped mode shapes, while bulb–frame intersections are assumed to remain ideally straight. As a result, the shear transfer path at these intersections is unaffected, even when longitudinal stiffeners are distorted. HS type C_{FP} is likewise unaffected, as the imperfections are located elsewhere. In contrast, HS type C_{NWT} displays variability caused by secondary bending effects in the GHGB load case.

The governing HS in GHGB loading is a Type C_{NWT}, located near the top of the bulb–frame connection, as shown in Figure 20. The corresponding stress decomposition in Figure 21 shows that SCF variability originates from the bending component, confirming that variability is driven by secondary bending effects associated with the straightening of longitudinal stiffeners under GHGB loading.

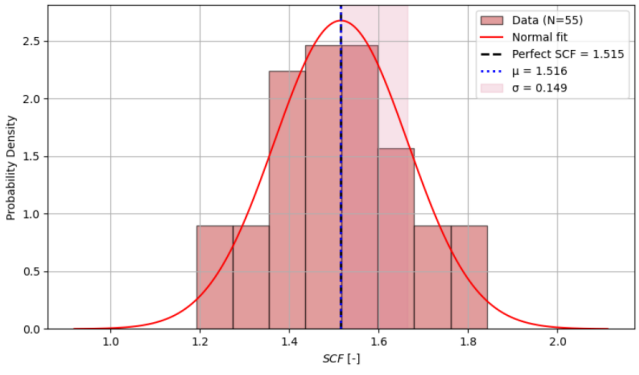

Figure 20: Governing SCF distribution for GHGB $f_{0,s}^{\text{long}}$ only

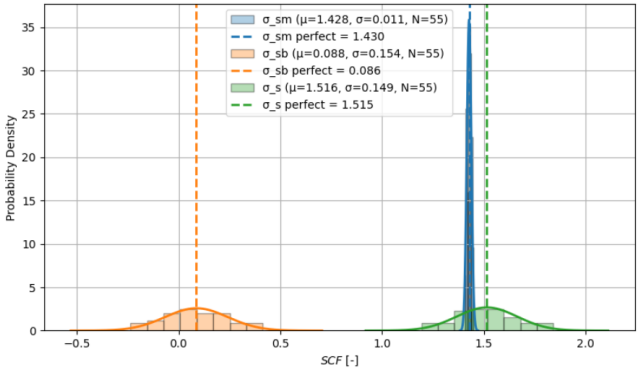

Figure 21: Membrane-, bending- and structural stress components HS Type C_{NWT}

4.7. Effect of Transversal Frame Distortion

The third series of simulations considers only the distortions of the transverse frame stiffeners, represented by the central third of a half sine wave. SCFs at the governing HS locations under both loading conditions are summarised in Table 7, alongside the corresponding SCFs for the idealised geometry.

Table 7
Results of the governing Hot Spot for f_{0s}^{trans} only

HS	Detail	Location	$\mathcal{N}(\mu_{SCF}, \sigma^2_{SCF})$	SCF$^{\text{ideal}}$
Water Pressure				
A	4	IV : b	$\mathcal{N}(2.24, 0.003^2)$	2.24
B	4	IV	$\mathcal{N}(0.93, 0.000^2)$	0.93
C_{NWT}	1	$z \approx 0.15$ m	$\mathcal{N}(2.30, 0.503^2)$	2.91
C_{FP}	-	$x = \frac{a}{2}$, $y \approx 1.5$ [m]	$\mathcal{N}(1.64, 0.012^2)$	1.64
Global Hull Girder Bending				
A	4	IV : b	$\mathcal{N}(0.37, 0.000^2)$	0.37
B	3	II	$\mathcal{N}(0.08, 0.000^2)$	0.08
C_{NWT}	6	$z \approx 0.05$ m	$\mathcal{N}(1.58, 0.234^2)$	1.61
C_{FP}	-	$x = \frac{a}{2}$, $y \approx 0.2$ [m]	$\mathcal{N}(1.02, 0.000^2)$	1.02

In the GHGB load case, the limited influence of transverse frame distortions on HS Types A and B is, similar to longitudinal stiffener distortions, primarily attributed to the assumed boundary conditions. In the present model, the u_z displacement is constrained at the lower outer edges of the frames. Relocating this constraint further away may increase the contribution of frame distortions, particularly for WP loading where the distortion direction aligns more closely with the applied load. In contrast, under GHGB loading the primary load direction is not aligned with the distortion direction, and no significant secondary bending is introduced, resulting in negligible SCF variation at these HS locations.

The type C_{NWT} HSs exhibit significant variability in both loading cases, with SCFs spanning tensile and compressive values. The results reported in Table 7 correspond

to the tensile SCFs. Figure 22 illustrates this behaviour for WP loading, together with normal fits through the tensile and compressive results. No consistent relation is observed between distortion direction and the sign of SCF in the GHGB loading scenario. In WP loading, however, a clear trend emerges: distortions in the positive x-direction correspond to tensile SCFs, while distortions in the negative x-direction correspond to compressive SCFs, when assessing the governing HSs of type C at the negative x-side of the frame–plate and frame–bulb connections.

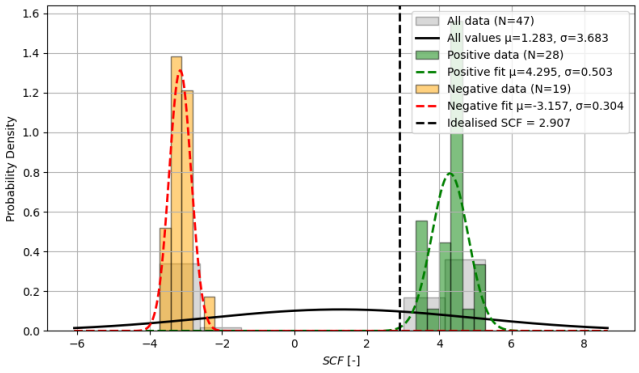

Figure 22: Normal distributions of tensile and compressive SCF values corresponding to f_{0s}^{trans} of HS type C_{NWT}

Additionally, although the influence on HS Types A and B is negligible at the governing locations, HS Type A at location I of the NWT details exhibits slight increases under WP loading. At this location (in reference to Figure 13), the distortion is considerably larger than at other NWT locations, which alters the shear load path and results in modest increases in SCFs as shown in Figure 23.

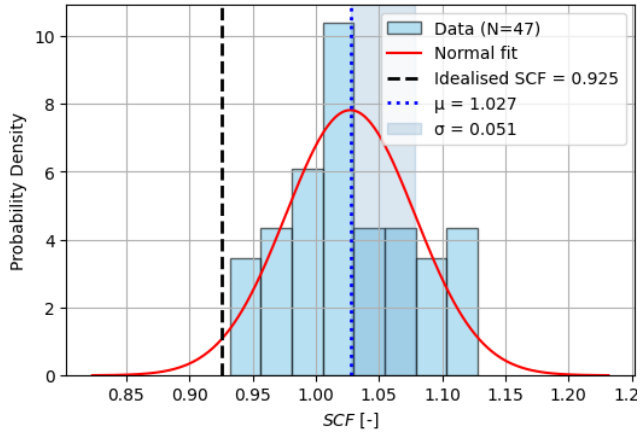

Figure 23: Increase of HS type A at location I corresponding to f_{0s}^{trans}

4.8. Effect of All Distortions

In the final simulation series, all previously defined geometric imperfections were applied simultaneously, including local plate distortions, longitudinal bulb distortions, and transverse frame distortions. Amplitude combinations were generated using Halton sequences to ensure uniform coverage of the input space and subsequently implemented in the finite element model. The resulting SCFs of the governing HSs for both loading conditions, together with those of the idealised geometry, are summarised in Table 8.

Table 8
Results of the governing Hot Spot for all distortions

HS	Detail	Location	$\mathcal{N}(\mu_{SCF}, \sigma^2_{SCF})$	SCF^{ideal}
Water Pressure				
A	1	IV : b	$\mathcal{N}(1.30, 0.057^2)$	2.24
B	1	IV	$\mathcal{N}(0.52, 0.025^2)$	0.93
C_{NWT}	6	$z \approx 0.15$ m	$\mathcal{N}(1.86, 0.209^2)$	3.74
C_{FP}	-	$x = \frac{a}{2}$, $y \approx 0.3$ [m]	$\mathcal{N}(1.65, 0.074^2)$	2.84
Global Hull Girder Bending				
A	4	IV : b	$\mathcal{N}(0.29, 0.012^2)$	0.37
B	4	I	$\mathcal{N}(0.11, 0.042^2)$	0.07
C_{NWT}	5	$z \approx 0.05$ [m]	$\mathcal{N}(1.57, 0.088^2)$	1.61
C_{FP}	-	$x = \frac{1.5a}{2}$, $y \approx 2.30$ [m]	$\mathcal{N}(1.92, 0.113^2)$	1.03

For WP loading, SCFs were consistently lower than those of the idealised configuration across all governing HSs. This trend mirrors the case with only local plate distortions, where mean SCFs decreased due to increased plate stiffness in distorted SHH realisations. At the type C_{NWT} HSs, however, the response is dominated by frame distortions, producing both tensile and compressive SCFs.

Under GHGB loading, the SCF response was more varied: some HSs showed reductions, while others exhibited increases relative to the idealised geometry. The type A and B HSs at the NWT detail remain largely unaffecte while the increases of the type C_{FP} HS are primarily caused by secondary bending effects induced by local plate distortions, and were observed at all assessed type C_{FP} locations. Transversal frame distortion dominates the type C_{FP} SCF distributions, while longitudinal bulb distortion contributes to the variability., where longitudinal bulb distortion contribute to the variability. The results are consistent with those obtained when only transversal frame distortions were modelled, in that both compressive and tensile SCFs occur. Table 8 reports only the tensile SCFs.

Although all presented results are based on static analyses, complementary nonlinear simulations revealed non-negligible deviations in SCF values, including both increases and decreases in stress levels. The associated standard deviations remained of similar magnitude, indicating that nonlinear analysis is recommended for accurate SCF prediction, particularly since secondary bending is inherently nonlinear, whereas static analysis is sufficient for quantifying SCF variability. d

4.9. Comparison with Guidelines and Standards

The framework enables a direct comparison of the distortion magnitudes and resulting SCFs from the benchmark studies with relevant fabrication tolerances and safety factors prescribed by classification society guidelines. This provides opportunities to assess whether guidelines adequately reflect unknown variability of imperfections in the design phase.

The assumed maximum distortion magnitudes of longitudinal stiffener sideways distortions adopt the *Limit* values from IACS No. 47, whereas transverse stiffener sideways distortions use the *Standard* values. For local plate distortions, the maximum amplitude is derived from the profiles of Ueda and Yao [19], with a mean value of 4.3 mm that slightly exceeds the IACS No. 47 limit of 4.0 mm and lies between the specified *Standard* and *Limit* ranges.

Existing fatigue assessment guidelines provide only limited coverage of the imperfections considered in this work, which are primarily welding-induced distortions. DNV [8] specifies additional safety factors only for plate butt welds, cruciform joints, and the gross geometry of the NWT detail, prescribing a value of 1.14 for the latter. BV [9] applies the same value for the same detail. No safety factors are provided for the specific imperfections modelled in the benchmark studies, and secondary bending effects are not addressed. As emphasised by Lillemäe [23], secondary bending should be incorporated in design guidelines, consistent with the present findings.

4.10. Bayesian Inference

To evaluate the performance of Bayesian inference within the proposed framework, posterior distributions were constructed for local plate distortion, as well as for the longitudinal and transverse stiffener distortions.

To establish the prior distribution for local plate distortion, measurement data from Panel 4 in [19] was excluded. This withheld panel was subsequently treated as newly observed data to update the prior and obtain the corresponding posterior distribution.

For the longitudinal and transverse stiffener distortions, the initial prior distributions were derived from the *Limit* tolerances specified in IACS No. 47. These priors were then updated using distortion measurements obtained via 3D laser scanning in [21]. However, the measured stiffeners in that study differ from those in the current configuration: the longitudinal stiffeners are discontinuous T-profiles, and the transverse stiffeners are approximately three times shorter. As a result, the new data used for updating may not be fully representative of the geometry analysed in this study.

Figure 24 illustrates the the Bayesian updating process for local plate distortion. The resulting prior and posterior distributions for all three imperfection types are summarised in Table 9.

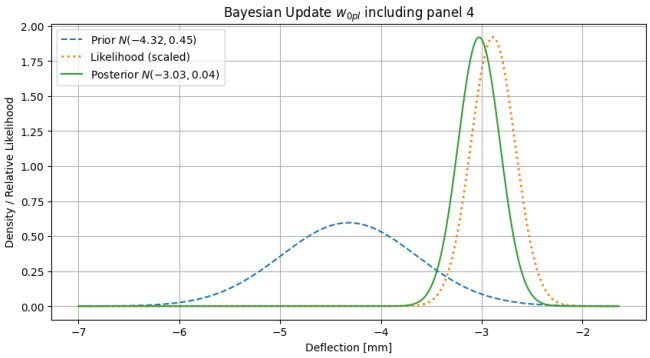

Figure 24: Bayesian update on local plate distortion including panel 4 [19]

Table 9
Prior and posterior distributions

Distortion	Prior [mm]	Posterior [mm]
$w_{0\text{pl}}$	$\mathcal{N}(4.32, 0.67^2)$	$\mathcal{N}(3.03, 0.21^2)$
$w_{0\text{s}}^{\text{long}}$	$\mathcal{N}(0.00, 4.30^2)$	$\mathcal{N}(-0.10, 0.03^2)$
$w_{0\text{s}}^{\text{trans}}$	$\mathcal{N}(0.00, 3.51^2)$	$\mathcal{N}(-0.10, 0.07^2)$

Using the *posterior* distributions, new imperfection fields are generated via the SRM and using an updated Halton sequence, and subsequently employed as input for the updated simulation framework.

Results

SCFs of the governing HSs for both loading conditions, alongside the SCF values for the idealised geometry, are summarised in Table 10. Figures 25 and 26 illustrate the corresponding governing SCF distributions based on prior and posterior imperfection inputs for WP and GHGB loading, respectively.

Table 10
Results of the governing Hot Spot for all imperfections

HS	Detail	Location	$\mathcal{N}(\mu_{SCF}, \sigma^2_{SCF})$	$\text{SCF}^{\text{ideal}}$
Water Pressure				
A	1	IV : b	$\mathcal{N}(2.07, 0.048^2)$	2.24
B	1	IV	$\mathcal{N}(0.84, 0.02^2)$	0.92
C_{NWT}	6	$z \approx 0.15$ m	$\mathcal{N}(2.08, 0.067^2)$	−1.79
C_{FP}	-	$x = \frac{a}{2}$, $y \approx 0.3$ [m]	$\mathcal{N}(2.57, 0.055^2)$	2.84
Global Hull Girder Bending				
A	4	IV : b	$\mathcal{N}(0.31, 0.004^2)$	0.37
B	1	I	$\mathcal{N}(0.09, 0.006^2)$	0.07
C_{NWT}	2	$z \approx 0.05$ m	$\mathcal{N}(1.37, 0.021^2)$	1.01
C_{FP}	-	$x = \frac{1.5a}{2}$, $y \approx 2.30$ [m]	$\mathcal{N}(1.67, 0.029^2)$	1.03

Similar to the prior distributions, the type C_{NWT} HSs show significant variability in the posterior distributions for both loading cases, with SCFs ranging from tensile to compressive values. The results reported in Table 10

correspond to the tensile SCFs.

Under WP loading, the posterior SCF distribution shifts closer to the idealised SCF value. This is primarily due to the updated local plate distortion distribution displaying both a lower mean and reduced variance, thereby reducing the extent of SCF reduction observed earlier. Furthermore, the posterior distributions for both the longitudinal and transversal stiffener distortions show variances approaching zero, minimising their respective influence.

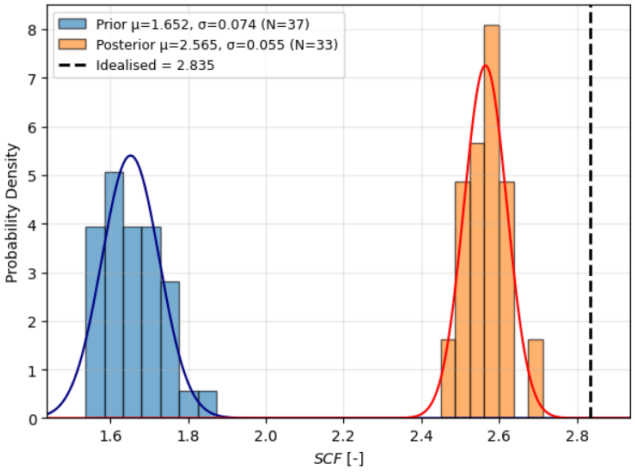

Figure 25: Prior and posterior distributions of governing SCF distribution for WP loading

A similar trend is observed under GHGB loading. The secondary bending effects introduced by the prior distributions are less pronounced in the posterior case, resulting in a reduced contribution to SCF magnitude and variation. Nevertheless, their combined presence still leads to an increase in the posterior mean SCF compared to the idealised configuration of the HSs type C.

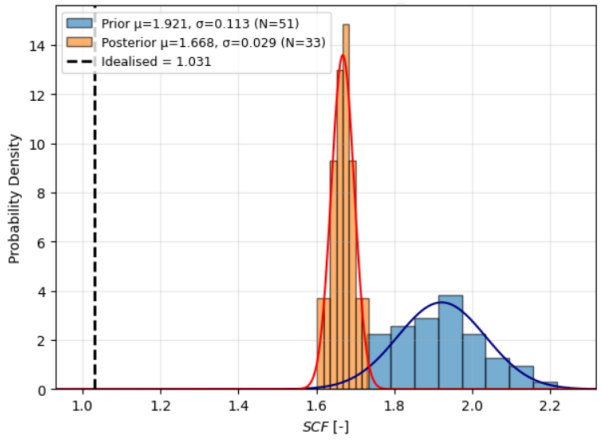

Figure 26: Prior and posterior distributions of governing SCF distribution for GHGB loading

5. Conclusions and Outlook

The probabilistic modelling framework developed in this study distinguishes between different types of geometric imperfections by treating some as random variables, such as stiffener distortions, global plate distortions, and plate thickness, and others as spatially varying random fields, such as local plate distortions. By combining these two representations, the framework effectively captures the inherent randomness of imperfections, even in the absence of an extensive measurement database.

A benchmark finite element study was conducted on a representative stiffened panel typical of bottom shell plating in ship structures, including realistic Non-Watertight (NWT) penetration details. Stochastic imperfections were implemented in `PyMAPDL` using `SHELL181` elements, and their effects were assessed both individually and in combination. Local plate distortions were found to reduce HS stresses under WP loading due to increased stiffness associated with the SHH profile, while GHGB amplified stresses as a result of straightening effects.

Longitudinal stiffener distortions, when isolated, showed limited influence when amplitudes were based on the *Standard* range of IACS No. 47. However, amplitudes from the *Limit* range produced significant variability in SCFs while leaving the mean value unaffected. Similar results were obtained for distortion shapes corresponding to clamped-clamped and simply-supported boundary conditions, indicating that the effect of longitudinal bulb stiffener distortions is governed primarily by magnitude rather than distortion shape.

Transversal stiffener distortions, represented by the central third of a sinusoidal half-wave, had a pronounced effect on HSs Type C at the bulb–frame connection. In both loading scenarios these distortions resulted in tensile as well as compressive SCF values at different locations. In GHGB no consistent trend was identified between distortion direction and SCF sign. In WP loading a clear relation was observed, where positive distortion directions corresponded to tensile SCFs and negative distortion directions corresponded to compressive SCFs in the local coordinate system of the benchmark study.

When all imperfections were applied simultaneously, SCFs consistently decreased in WP loading, dominated by the effect of local plate distortions, while GHGB produced both decreases, and increases due to secondary bending. These findings demonstrate that imperfections do not necessarily degrade fatigue performance and may, in some cases, reduce local stresses.

The present results are based on static analyses. Complementary nonlinear simulations indicated that mean SCFs increased while variability remained of similar magnitude. This suggests that nonlinear analysis is recommended for accurate SCF prediction, whereas static analysis is sufficient for quantifying SCF variability.

The findings highlight a gap in current fatigue assessment guidelines, such as DNV [8] and BV [9], which do not provide safety factors for welding-induced distortions and fail to account for secondary bending effects. This suggests that current standards may underestimate the influence of as-built distortions on fatigue-critical stresses. More broadly, existing standards focus primarily on gross misalignments and geometric deviations, while overlooking local plate distortions and stiffener sideways distortions that introduce SCF variability not currently addressed. In particular, governing HS Type C results revealed significantly elevated SCFs due to secondary bending, an effect absent from current guidelines but, as also recognised by Lillemäe [23], essential to include.

The developed framework combines physical modelling with efficient uncertainty quantification, using Halton sequences to sample the high-dimensional imperfection space without the computational cost of full factorial approaches. It is the first to integrate SRM-based local imperfections, quasi-random Halton sampling, and Bayesian inference for (arc-)welded maritime structures within the context of fatigue assessment. The inclusion of Bayesian updating enables systematic incorporation of fabrication data, such as 3D laser scans, allowing for yard- or process-specific fatigue assessments and supporting a shift toward data-driven fatigue resistance evaluation. The findings demonstrate the value of a stochastic approach that captures the inherent variability in fabrication and assembly processes. They also show that deterministic models based on idealised geometries, as assumed in current design guidelines, can either overpredict or underpredict fatigue-critical HS stresses depending on the loading conditions and imperfections present.

Several recommendations arise from this work. First, to validate the adopted distortion profiles and statistically characterise distortion magnitudes, a benchmark investigation on a real structure using three-dimensional laser scanning should be carried out to provide direct validation of the simulation results. In the present benchmark study, stiffener sideways distortions and local plate distortions were treated as statistically independent. It is, however, expected that stiffener distortion amplitudes and adjacent plate fields follow joint probability density functions. Once a sufficiently large measurement database becomes available, such joint distributions can be established and applied as input, enabling the results to more accurately reflect as-built statistical behaviour. Furthermore, if representative measurement data are obtained that capture local spatial variability in distortion profiles, these should be incorporated using a random field theory-based approach. This is particularly relevant for imperfections associated with weld geometry and stiffener profiles, where local spatial variation is expected to significantly influence the local structural stress response.

To improve accuracy of hot spot stress assessments, welding residual stresses should be included through thermo-mechanical analyses. The input variables of this thermo-mechanical analyses should be treated in a probabilistic manner to remain consistent with the probabilistic context of this work. Accuracy should be further improved by modelling the weld with inclined shells or applying a substructure approach in which local solid models simulate imperfections related to weld geometry. This substructure approach could complement the current Hot Spot Structural Stress method by the Averaged Effective Notch Stress Concept to better account for size effects and geometric details at HS locations.

Another recommendation is to improve the representation of boundary conditions. In the benchmark study, the u_z displacement was constrained only at the bottom of the frames. Future simulations should constrain the u_z displacement along the full web height, as shear transfer occurs over the entire height rather than at a single point.

The probabilistic framework should be extended to include further imperfections such as linear misalignments, weld geometry irregularities, and distortions in stiffener webs and flanges. A dedicated sensitivity study is recommended to establish technically justified acceptance limits for fabrication tolerances given in ISO 5817 and IACS No. 47. This study should examine the influence of varying boundary conditions and measured distortion profiles on fatigue performance, using the same cutout details but with different dimensions of the associated plate fields and associated stiffener profiles.

6. Acknowledgements

This work was carried out as part of the FReady project and performed at Nevesbu. I would like to express my gratitude to Pieter Nobel and Alessandro Zambon for their warm welcome at Nevesbu and for their excellent supervision and insightful discussions, which greatly contributed to this work. My time at the Nevesbu office felt like it flew by thanks to their support. I would also like to thank Henk den Besten for his valuable guidance and critical perspective. His mindful and knowledgeable questions consistently helped to sharpen my thinking and move the work forward. Finally, I am deeply grateful to Ruben Slange for his dedicated supervision. Our frequent and in-depth discussions played a significant role in shaping this work, and his continuous support has been invaluable. I would further like to acknowledge TNO for their discussions throughout this project.

References

[1] J. Schijve, Fatigue of Structures and Materials, Springer Dordrecht, 2009. doi:https://doi.org/10.1007/978-1-4020-6808-9.

[2] W. Mao, I. Rychlik, G. Storhaug, Safety index of fatigue failure for ship structure details, Journal of Ship Research 54 (2010) 197–208.

[3] Y. Qin, J. den Besten, S. Palkar, M. Kaminski, Mid-and high-cycle fatigue of welded joints in steel marine structures: effective notch stress and total stress concept evaluations, International Journal of Fatigue 142 (2021) 105822.

[4] Y. Qin, J. den Besten, S. Palkar, M. Kaminski, Fatigue design of welded double-sided t-joints and double-sided cruciform joints in steel marine structures: A total stress concept, Fatigue & Fracture of Engineering Materials & Structures 42 (2019) 2674–2693.

[5] J. den Besten, Fatigue resistance of welded joints in aluminium high-speed craft: a total stress concept, Phd thesis, Delft University of Technology, 2015. doi:http://dx.doi.org/10.4233/uuid:370b3d44-f4a6-403e-9629-d36174c3aca4.

[6] J. Schijve, G. Campoli, A. Monaco, Fatigue of structures and secondary bending in structural elements, International Journal of Fatigue 31 (2009) 1111–1123.

[7] Y. Dong, Y. Garbatov, C. Soares, Review on uncertainties in fatigue loads and fatigue life of ships and offshore structures, Ocean Engineering 264 (2022) 112514.

[8] Fatigue Assessment of ship structures, Det Norske Veritas (DNV), Høvik, Norway, 2021.

[9] Guideline for Fatigue Assessment of Ships and Offshore Units, Bureau Veritas (BV), Paris, France, 2020.

[10] Eurocode 3: Design of steel structures - Part 1-9: Fatigue, NEN-EN, 2021.

[11] Shipbuilding and Repair Quality Standard, International Association of Classification Societies (IACS), London, England, 2021.

[12] Welding — Fusion-welded joints in steel, nickel, titanium and their alloys (beam welding excluded) — Quality levels for imperfections, NEN-EN-ISO, 2023.

[13] J. Baumgartner, Review and considerations on the fatigue assessment of welded joints using reference radii, International Journal of Fatigue 101 (2017) 459–468.

[14] H. Bartsch, M. Feldmann, Fatigue strength of cruciform joints with weld imperfections: A comprehensive numerical study, Engineering Failure Analysis 157 (2024) 107866.

[15] D. Georgiadis, M. Samuelides, Stochastic geometric imperfections of plate elements and their impact on the probabilistic ultimate strength assessment of plates and hull-girders, Marine Structures 76 (2021) 102920.

[16] A. Antoniou, On the maximum deflection of plating in newly built ships, Journal of ship research 24 (1980) 31–39.

[17] L. Eggert, W. Fricke, H. Paetzold, Fatigue strength of thin-plated block joints with typical shipbuilding imperfections, Welding in the World 56 (2012) 119–128.

[18] J. W. Ringsberg, I. Darie, K. Nahshon, G. Shilling, M. A. Vaz, S. Benson, L. Brubak, G. Feng, M. Fujikubo, M. Gaiotti, et al., The issc 2022 committee iii. 1-ultimate strength benchmark study on the ultimate limit state analysis of a stiffened plate structure subjected to uniaxial compressive loads, Marine structures 79 (2021) 103026.

[19] Y. Ueda, T. Yao, The influence of complex initial deflection modes on the behaviour and ultimate strength of rectangular plates in compression, Journal of Constructional Steel Research 5 (1985) 265–302.

[20] M. Yi, C. Hyun, J. Paik, Full-scale measurements of welding-induced initial deflections and residual stresses in steel-stiffened plate structures, International Journal of Maritime Engineering 160 (2018).

[21] M. Yi, D. Lee, H. Lee, J. Paik, Direct measurements and numerical predictions of welding-induced initial deformations in a full-scale steel stiffened plate structure, Thin-Walled Structures 153 (2020) 106786.

[22] J. K. Paik, A. K. Thayamballi, Ultimate limit state design of steel-plated structures, John Wiley & Sons, 2003.

[23] I. Lillemäe, Fatigue assessment of thin superstructure decks, Phd thesis, 2014.

[24] F. Mancini, Enhancing the structural stress assessment of distorted lightweight ship deck structures, Phd thesis, Aalto University, 2024. doi:https://urn.fi/URN:ISBN:978-952-64-1869-8.

[25] O. Hughes, J. Paik, Ship Structural Analysis and Design, 2010.

[26] S. Li, D. Georgiadis, M. Samuelides, D. K.K., A comparison of geometric imperfection models for collapse analysis of ship-type stiffened plated grillages, Engineering Structures 250 (2022) 113480.

[27] F. Mancini, H. Remes, J. Romanoff, On the modelling of distorted thin-walled stiffened panels via a scale reduction approach for a simplified structural stress analysis, Thin-Walled Structures 197 (2024) 111637.

[28] R. Maquoi, M. Skaloud, Stability of plates and plated structures: General report, Journal of Constructional Steel Research 55 (2000) 45–68.

[29] Z. Man, W. Song, J. Xu, S. Wei, M. Cui, X. Shi, F. Berto, Misalignment effect on the fatigue failure behavior of load-carrying cruciform welded joints, International Journal of Fatigue 160 (2022) 106847.

[30] I. Lillemäe, H. Lammi, L. M., H. Remes, Fatigue strength of welded butt joints in thin and slender specimens, International Journal of Fatigue 44 (2012) 98–106.

[31] H. Bartsch, M. Feldmann, Fatigue class combination model to quantify the influence of multiple weld imperfections on fatigue strength, Journal of Constructional Steel Research 222 (2024) 108930.

[32] D. Schillinger, V. Papadopoulos, M. Bischoff, M. Papadrakakis, Buckling analysis of imperfect i-section beam-columns with stochastic shell finite elements, Computational Mechanics 46 (2010) 495–510.

[33] B. Sudret, A. Der Kiureghian, Stochastic finite element methods and reliability: A state-of-the-art report (2000).

[34] M. Grigoriu, On the spectral representation method in simulation, Probabilistic Engineering Mechanics 8 (1993) 75–90.

[35] B. Zhu, D. Frangopol, Reliability assessment of ship structures using bayesian updating, Engineering Structures 56 (2013) 1836–1847.

[36] D. Straub, I. Papaioannou, Bayesian updating with structural reliability methods, Journal of Engineering Mechanics 141 (2015) 04014134.

[37] L. Kocis, W. J. Whiten, Computational investigations of low-discrepancy sequences, ACM Transactions on Mathematical Software (TOMS) 23 (1997) 266–294.

[38] M. Pharr, W. Jakob, G. Humphreys, Sampling and reconstruction, in: Physically Based Rendering, third edition ed., Morgan Kaufmann, 2017, pp. 401–504. doi:10.1016/B978-0-12-800645-0.50007-5.

[39] P. Dong, A structural stress definition and numerical implementation for fatigue analysis of welded joints, International journal of fatigue 23 (2001) 865–876.

[40] P. Dong, A robust structural stress method for fatigue analysis of ship structures, in: International Conference on Offshore Mechanics and Arctic Engineering, volume 36835, 2003, pp. 199–211.